This is a preprint, the final version is subject to change, of the American Mineralogist (MSA)
Cite as Authors (Year) Title. American Mineralogist, in press.
(DOI will not work until issue is live.) DOI: http://dx.doi.org/10.2138/am-2016-5729

REVISION 1

Study on nanophase iron oxyhydroxides in freshwater ferromanganese nodules from Green Bay, Lake Michigan

Seungyeol Lee, Zhizhang Shen, and Huifang Xu*

NASA Astrobiology Institute, Department of Geoscience, University of Wisconsin–Madison, Madison, Wisconsin 53706

* Corresponding author:
Prof. Huifang Xu,
Department of Geoscience,
University of Wisconsin-Madison
1215 West Dayton Street, A352 Weeks Hall
Madison, Wisconsin 53706
Tel: 1-608-265-5887
Fax: 1-608-262-0693
Email: hfxu@geology.wisc.edu

This is a preprint, the final version is subject to change, of the American Mineralogist (MSA)
Cite as Authors (Year) Title. American Mineralogist, in press.
(DOI will not work until issue is live.) DOI: http://dx.doi.org/10.2138/am-2016-5729

ABSTRACT

Nanophase Fe-oxyhydroxides in freshwater ferromanganese nodules (FFN) from Green Bay, Lake Michigan and adsorbed arsenate have been investigated by X-ray powder diffraction (XRD), high-resolution transmission electron microscopy (HRTEM), Z-contrast imaging, and *ab-initio* calculations using the density functional theory (DFT). The samples from northern Green Bay can be divided into two types: Fe-Mn nodules and Fe-rich nodules. The manganese-bearing phases are todorokite, birnessite, and buserite. The iron-bearing phases are feroxyhyte, nanophase goethite, 2-line ferrihydrite, and nanophase FeOOH with guyanaite structure. Z-contrast images of the Fe-oxyhydroxides show ordered FeOOH nano-domains with guyanaite structure intergrown with nanophase goethite. The FeOOH nanophase is a precursor to the goethite. Henceforth, we will refer to it as "proto-goethite". DFT calculations indicate that goethite is more stable than proto-goethite. Our results suggest that ordering between Fe and vacancies in octahedral sites result in the transformation from feroxyhyte to goethite through a proto-goethite intermediate phase. Combining Z-contrast images and TEM-EDS reveals that arsenate (AsO_4^{3-}) tetrahedra are preferentially adsorbed on the proto-goethite (001) surface via tridentate adsorption. Our study directly shows the atomic positions of Fe-oxyhydroxides with associated trace elements. The methods can be applied for identifying structures of nano-phases and adsorbed trace elements and heavy metals.

Keywords: XRD, HRTEM, Z-contrast imaging, *ab-initio*, 2-line ferrihydrite, proto-goethite, nanophase goethite, feroxyhyte, ferromanganese nodule, arsenic

1. INTRODUCTION

Freshwater ferromanganese nodules (FFN) are found in lakes throughout the northern temperate latitudes and are often associated with glacial debris (Rossmann and Callender 1968). Glaciated regions around Green Bay, Lake Michigan contain sediments derived from Precambrian rocks that may be plentiful sources of iron, manganese, and trace elements (Rossmann and Callender 1968). Dissolved metals from glacier-derived sediments contribute to the formation and chemistry of the Green Bay FFN on the surficial sediments, where sedimentation rates are low (Callender et al. 1973). Previous studies of Green Bay nodules provide information on their mineralogy, occurrence, bulk chemical composition, and bacterial population relationships (Rossmann and Callender 1968; Edgingto and Callender 1970; Robbins and Callender 1975; Christensen and Chien 1981; Rossmann and Edgington 2000; Stein et al. 2001). However, few studies have addressed nanophase Fe minerals and their trace-element binding behavior in Green Bay nodules (Stein et al. 2001). In contrast, ocean ferromanganese nodules have been actively discussed because they are more likely to be economically viable ore deposits and they contain much higher concentrations of trace metals than those formed in the freshwater environment (Marcus et al. 2004; Novikov and Bogdanova 2007; Feng et al. 2012; Atkins et al. 2014; Manceau et al. 2014a).

Green Bay nodules contain nanophase Fe-oxyhydroxides: feroxyhyte, nanophase goethite, and 2-line ferrihydrite (Callender et al. 1973). The nature of some of the iron oxyhydroxides is still perplexing due to their highly defective and disordered crystal structures. Nanophase goethite is reported to be the major Fe-oxyhydroxide in lacustrine environments (Fontes et al. 1992; Manceau et al. 2003; Handler et al. 2009). Feroxyhyte has a disordered structure with cations distributed semi-randomly over the anion interstices (Drits et al. 1993a). The feroxyhyte generally occurs with its polymorphs, nanophase goethite

(Koch et al. 1995; Majzalan et al. 2008). Ferrihydrite, a common Fe-oxyhydroxide mineral in oxidized sediments, exists as highly defective nanoparticles (Drits et al. 1993b; Michel et al. 2007a; Manceau 2009; Harrington et al. 2010; Parise et al. 2010). The structure of ferrihydrite is still controversial (Michel et al. 2007; Harrington et al. 2010; Parise et al. 2010; Manceau 2011; Manceau et al. 2014b).

Nanophase iron oxyhydroxides have large surface areas and high chemical activity, both of which contribute significantly to the adsorption of trace elements (Cornell and Schwertmann 2003; Marcus et al. 2004; Barron and Torrent 2013). Previous studies revealed that Fe-oxyhydroxides preferentially incorporates As, U, and V (Nowlan 1976; Palumbo et al. 2001; Koschinsky and Hein 2003; Manceau et al. 2007a; Manceau et al. 2014a). The preference of oceanic ferromanganese nodules for adsorption of As(V) is well known (Palumbo et al. 2001; Marcus et al. 2004; Manceau et al. 2007a; Manceau et al. 2014a), but the adsorption behavior with respect to As(V) of freshwater ferromanganese nodules are much less studied (Callender et al. 1973; Manceau et al. 2007b).

The goal of this study is to better understand the occurrence of nanophase Fe-oxyhydroxides and their incorporation of arsenate in freshwater ferromanganese nodules from Green Bay, Lake Michigan. We used X-ray powder diffraction (XRD), high-resolution transmission electron microscopy (HRTEM), scanning transmission electron microscopy (STEM), and *ab-initio* using density functional theory (DFT) calculations to examine the nanophase mineralogy and the As(V) behavior in nanophase iron oxyhydroxides. We observed feroxyhyte, nanophase goethite, 2-line ferrihydrite, and nanophase FeOOH with guyanaite structure, a precursor to goethite. The proto-goethite (intermediate phase between feroxyhyte and goethite) was the main focus of Z-contrast images and *ab-initio* calculations in order to determine its structure, thermodynamic stability, and adsorption behavior towards

93 As(V).

94

95 **2. SAMPLES AND METHODS**

96 **2.1 Freshwater ferromanganese nodules**

97 The selected FFN samples for this study were previously studied by Callender et al.
98 (1973). Samples were collected from the uppermost ~10 cm of lake-bottom sediments in the
99 northern Green Bay, Lake Michigan (Fig. 1). Callender et al. (1973) proposed that the
100 different solubility of Fe and Mn from sediments' weathering products may be the primary
101 control on the Green Bay FFN chemistry. Green Bay nodules vary in diameter from 0.5 to 5
102 mm and can be divided into two types: Fe-Mn nodules and Fe-rich nodules (Fig. 2). Fe-Mn
103 nodules consist of both black Mn-oxides and reddish brown Fe-oxyhydroxides (Fig. 2A). Fe-
104 rich nodules are more spherical and are dominated by yellowish and red-brownish Fe-
105 oxyhydroxides (Fig. 2B).

106

107 **2.2 Experimental methods**

108 We prepared the polished thin sections with a thickness of 50 μm for XRD analysis. X-
109 ray diffraction patterns were collected on 2-D image-plate detector by using a Rigaku Rapid
110 II instrument (Mo-Kα radiation) in the Geoscience Department at the University of
111 Wisconsin-Madison. Two dimensional images were converted to produce conventional 2θ vs.
112 intensity patterns using Rigaku's 2DP software. Sections of nodules were analyzed from the
113 inner part to outer layer using a 0.3 mm diameter collimator. X-ray diffraction data were
114 compared with published data for natural 2-line ferrihydrite, including reference files of
115 goethite (PDF#00-029-0713), feroxyhyte (PDF#00-013-0087), birnessite (PDF#00-043-
116 1456), buserite (PDF#00-032-1128), and todorokite (PDF#00-038-0475).

High-resolution TEM images and selected-area electron diffraction (SAED) analyses were performed using a Philips CM200-UT microscope operated at 200 kV equipped with GE light-element energy-dispersive X-ray spectrometer (EDX) in the Materials Science Center at the University of Wisconsin-Madison. Z-contrast images were carried out using an FEI Titan 80-200, operated at 200 kV and equipped with an EDAX high-resolution EDS detector and a Gatan image filtering system. This instrument is capable of imaging single atoms with ~0.1 nm spatial resolution in STEM mode (Xu et al. 2014a). The STEM method uses the high-angle annular dark-field (HAADF) detector to support the most highly localized 1s Bloch state imaging (Pennycook et al. 2000). The Z-contrast imaging is a powerful tool for determining crystal structures, vacancies, and other defects (Shen et al. 2014; Xu et al. 2014b).

Ab-initio calculations were implemented in the Vienna *ab-initio* simulation package (VASP, (Kresse and Furthmuller 1996)). The general gradient approximation (GGA) with the Perdew, Burke, and Ernzerhof (PBE) parameters was employed (Perdew et al. 1996). The projector-augmented wave (PAW) method with an energy cutoff of 700 eV was used. The PAW potentials were generated with the following valence electronic configurations: $3p^6 3d^7 4s^1$ for Fe and $2s^2 2p^4$ for O. K-point meshes of 48 irreducible k-points were used for calculations. The electronic SCF-spell out convergence tolerance (EDIFF) was set to 10^{-5}. The systems were first fully relaxed in terms of internal coordinates, unit-cell volume and shape. Then, static calculations were performed to obtain the ground state energy of each system. In order to consider the on-site Coulomb interactions of the 3d electrons in Fe atoms, a GGA+U method described by Dudarev et al. (1998) was employed. The parameters were set at U = 4 eV and J = 1 eV as previously used for the calculations of Fe-oxyhydroxides (Pinney et al. 2009). Spin-polarized calculations were performed with initial

antiferromagnetic magnetic configurations (Cornell and Schwertmann 2003). The zero-point energies (ZPEs) for proto-goethite and goethite were approximated by the vibrational frequencies of the H atoms.

3. RESULTS AND DISCUSSION

3.1 Mineralogy of nanophase Fe-oxyhydroxides

Major diffraction peaks at 4.18 Å $(110)_{Gt}$, 2.69 Å $(130)_{Gt}$, 2.45 Å $(111)_{Gt}$, and 1.71 Å $(221)_{Gt}$ indicate the presence of nanophase goethite (Fig. 3). Diffraction patterns of feroxyhyte contain four main peaks at 2.55 Å $(100)_{Fxy}$, 2.23 Å $(101)_{Fxy}$, 1.70 Å $(102)_{Fxy}$, and 1.47 Å $(110)_{Fxy}$ (Fig. 3). Both nodules show two broad humps in the background, centered at ~2.6 Å and ~1.5 Å, indicating the presence of 2-line ferrihydrite (Fig. 3). The identified manganese phases are todorokite, birnessite, and buserite (Fig. 3). The mineralogy of nanophase Mn-oxide in Green Bay nodules is specifically discussed in Lee and Xu (2016).

The TEM images and SAED patterns confirm the presence of nanophase Fe-oxyhydroxides (Fig. 4). A low-magnification TEM image shows aggregated 2-line ferrihydrite with the SAED pattern showing two broad diffraction rings corresponding to ~2.5 Å and ~1.5 Å (Fig. 4A). Figure 4B shows aggregates of goethite and 2-line ferrihydrite nanocrystals with their SAED pattern. The HRTEM image shows lattice fringes of the goethite nanoparticles and pseudo-hexagonal lattice fringes from feroxyhyte or proto-goethite (Fig. 4C). Hexagonal shaped nano-crystals of disordered Fe-oxyhydroxide (feroxyhyte) display ~2.5 Å lattice fringes parallel to the edges of the crystal (Fig. 4D). X-ray energy dispersive spectra show that disordered Fe-oxyhydroxides contain more Si, P, Ca and trace elements As and Ni than the goethite-rich domains (Figs. 4E and 4F).

The Z-contrast image (Fig. 5) directly shows the positions of Fe (bright spots), whereas

positions of oxygen and hydrogen are omitted for clarity because their scattering of electrons is much weaker than that from Fe atoms. The noise-filtered Z-contrast image of the ordered domain and its fast Fourier transform (FFT) pattern show the hexagonal arrangement of Fe-positions (Fig. 5). The [001]-zone-axis of FeOOH with guyanaite structure (i.e. proto-goethite), feroxyhyte, and hematite can explain the observed hexagonal arrangement of Fe atoms; however the observed hexagonal distribution of Fe atoms does not occur in goethite along any direction (Fig. 6). The ideal feroxyhyte model shows the hexagonal pattern of Fe atoms along the *c*-axis, however, the cation positions of feroxyhyte are disordered and distributed semi-randomly over the anion packing (Drits et al. 1993b). Hematite is not a possible phase since it is not detected by XRD and HRTEM.

A [010]-zone-axis Z-contrast image shows domains of nanophase goethite and proto-goethite (Fig. 7). Upper and central areas show nano-domains of FeOOH with the guyanaite structure (proto-goethite) intergrown with the goethite since the Fe atoms of both goethite and proto-goethite overlap along the *b*-axis (Fig. 7). A proposed model illustrated in Figure 8 matches well with the Z-contrast domains (Figs. 7 and 8). The Z-contrast image (Fig. 7) indicates a (010) interface between nanophase goethite and proto-goethite through edge-sharing (Fig. 8). On the contrary, hematite and feroxyhyte models cannot explain the observed Z-contrast image along any direction.

We carried out *ab-initio* calculations using the DFT method to obtain detailed atomic positions of the proto-goethite and relative energies of the FeOOH polymorphs. Polymorphs of FeOOH are generally orthorhombic (goethite, lepidocrocite, and γ-FeOOH) and pseudo-tetragonal (akaganéite and β-FeOOH) (Rosso and Rustad 2001; Cornell and Schwertmann 2003). Although several structures of FeOOH polymorphs have been recognized, the energetic relations among them remain controversial (Laberty and Navrotsky 1998; Rosso

and Rustad 2001).

The proto-goethite structure calculated for 0 K is shown in Table 1 and is based on the space group of $Pm2_1n$. Proto-goethite has the same chemical composition as goethite (α-FeOOH), but it is made up of single chains of edge-sharing FeO_6 octahedra (Fig. 8). The structure resembles high-pressure phases of FeOOH and InOOH (Chenavas et al. 1973; Cornell and Schwertmann 2003). Proto-goethite consists of oxygen and hydroxyl sheets stacked in hexagonal (ABAB) sequences along the ***c***-axis, and Fe atoms occupy 50% of the octahedral sites in each layer (Fig. 8). The overlay of the Z-contrast image with the structure model of proto-goethite along the [001]-zone-axis and [010]-zone-axis (Figs. 5B and 7C) illustrates the good agreement between the two.

The unit-cell parameters of the calculated goethite and proto-goethite (Table 2) are close to previous experimental data (Chenavas et al. 1973; Gualtieri and Venturelli 1999). The larger difference between the calculated and experimental values for akaganéite arises from the presence of chloride in its structure (Post et al. 2003). The calculated energy of goethite is the lowest among the four FeOOH polymorphs (Table. 3 and Fig. 9A), and the relative energies of proto-goethite, lepidocrocite and akaganéite with respect to goethite are 5.61, 13.03, and 27.35 kJ/mol, respectively. The calculated H vibrational wavenumbers for goethite and proto-goethite are 2864 cm^{-1}, 1009 cm^{-1}, 920 cm^{-1} and 2401 cm^{-1}, 1238 cm^{-1}, 1046 cm^{-1}, respectively. The values for goethite are in agreement with previous IR experimental data (Christensen and Christensen 1978; Pinney et al. 2009). Calculated zero-point energies (ZPEs) are 28.67, 28.02, 28.85 and 29.96 kJ/mol per H atom for goethite, proto-goethite, lepidocrocite and akaganéite, respectively (Table. 3). The calculated ZPE for goethite (28.7 kJ/mol per H atom) is slightly lower than a previous calculation (29.6 kJ/mol per H atom) (Pinney et al. 2009). Including this ZPE corrections, goethite is the most stable phase. The

213 calculated relative stabilities is overall similar to the experimental data (Laberty and
214 Navrotsky 1998) (Fig. 9A) and earlier DFT results (Rosso and Rustad 2001). However,
215 compared to Rosso and Rustad data, our results predict that proto-goethite is slightly less
216 stable than goethite (Fig. 9A). Goethite should be the most stable polymorph based on its
217 occurrence in nature. It is likely that a disordered structure of feroxyhyte will have higher
218 energy than proto-goethite, although its exact energy position is not constrained.

219 The XRD data, Z-contrast images, and DFT calculations allow to depict the formulate
220 transformation pathway models for the three Fe-oxyhydroxides (Fig. 9B). The structures of
221 feroxyhyte, proto-goethite, and goethite are based on a hexagonal close-packed arrangement
222 of O-atoms with Fe distributed over half of the octahedral sites (Fig. 9B). Z-contrast images
223 identified ordered domains and less ordered domains (Fig. 5), which may indicate
224 transformation from feroxyhyte to proto-goethite. Z-contrast imaging (Fig. 7) shows proto-
225 goethite domains within a goethite host. *Ab-initio* calculations suggest that goethite is more
226 stable than proto-goethite (Table. 3 and Fig. 9A). Therefore, Fe ordering results in the
227 transformation from feroxyhyte to goethite via a proto-goethite intermediate phase (Fig. 9B).

228 The [010]-zone-axis Z-contrast image illustrates goethite stacking faults with a stackin
229 g vector of ~1/2[**b**+**c**] (Figs. 7C and Fig 10). An atomic model of goethite stacking faults is
230 overlaid on the Z-contrast image (Fig. 7C). The stacking fault causes the displacement of
231 double chains of Fe-O octahedra (Fig. 10).

232 Proto-goethite phase is identified in XRD patterns from Green Bay nodules (Fig. 11). A
233 broad peak at ~3.3 Å (overlap with a sharp (101) quartz peak) represents the proto-goethite
234 (011) diffraction (Figs. 11A and 11D). The other diffraction peaks of proto-goethite are
235 overlapped with peaks from feroxyhyte and nanophase goethite (Fig. 11).

236

3.2 As speciation on nanophase Fe-oxyhydroxides

High As concentrations in Green Bay FFN were reported in previous studies (Callender et al. 1973; Stein et al. 2001). In most freshwater environments with a pH range from 6 to 8, Fe-oxyhydroxides carry a weak positive charge on the surface (Stumm 1987). As a result, the negative arsenate (AsO_4^{3-}) ion can potentially interact with the Fe-oxyhydroxide surfaces. Callender et al. (1973) reported a positive Fe-As correlation in Green Bay FFN, and they showed that the As concentration in the outer layers was higher than in the inner part (Callender et al. 1973). Our TEM-EDS results show that As is strongly associated with proto-goethite phases (Fig. 4E) instead of nanophase goethite (Fig. 4F), suggesting that immature outer layers contain more As due to the greater amounts of proto-goethite and feroxyhyte.

A [001]-zone-axis Z-contrast image of proto-goethite shows the adsorbed As (bright spots) and Fe (less bright spots) (Fig. 12A). The intensity profile diagram from an outlined area shows similar ratios ($I_{7Fe} : I_{8Fe} : I_{As+7Fe+O} = 1 : 1.14 : 1.40$) in the simulated STEM image (Figs. 12B, 12C, and 12D). The Z-contrast image suggests that As tetrahedra are adsorbed on the proto-goethite (001) surface via a tridentate complex (Figs. 12E and 12F). The sequence of 7Fe atoms and 8Fe atoms support the guyanaite structure of proto-goethite (Fig. 12B). We can estimate the approximate sample thickness (~3nm) of proto-goethite based on the number of Fe atoms. The single chain of proto-goethite structurally favors AsO_4^- through the tridentate complex than the bidentate complex on goethite (Fig. 13), and consequently poorly crystalline outer layers can contain more arsenic. The structure of proto-goethite is also preferentially able to adsorb other tetrahedra (SiO_4, PO_4, and SO_4) on the (001) surface via in tridentate complex (Fig. 13). While the P may be adsorbed by a similar mechanism, Z-contrast imaging is not sensitive enough to reveal atoms of low atomic number.

IMPLICATIONS

Results from TEM, Z-contrast imaging, and *ab-initio* calculations clarify the nature of the crystal structure and chemistry of nanophase Fe-oxyhydroxides. Z-contrast images and image simulation successfully show the atomic positions of nanophases and their associated trace elements since the instrument can image single atoms (sub-Å resolution) with aberration-corrected STEM. The methods can be applied to enhance the understanding of nano-crystal structure, nanophase transformation, and adsorbed trace elements and heavy metals. For example, nanosized Fe-oxyhydroxides have a large adsorption capacity in the control of accumulation and distribution of many toxic elements such heavy metals and radionuclides. The methods will have potential implications in environmental science for understanding anisotropic adsorption on mineral surfaces and possible roles of mineral surfaces in controlling adsorbed heavy metals. Z-contrast imaging is sensitive in revealing heavy metals in or on light matrix materials.

The nanophase Fe-oxyhydroxides in Green Bay nodules have similar mineralogical properties with the amorphous component of Mars soils. The CheMin XRD patterns and the chemical composition of the amorphous component of Rocknest, John Klein, and Cumberland, Mars suggest that nanophase Fe-oxyhydroxides are present and abundant (Bish et al. 2013; Blake et al. 2013; Vaniman et al. 2014). It is evidenced in the XRD patterns by the elevated background between 14º (7.32 Å) to 53º (2.00 Å) (Supplementary Fig. S1). Diffraction patterns of Green Bay nodules have the background between ~5.1 Å and ~2.0 Å (Figs. 3 and 11), as a result of nanophase Fe-oxyhydroxides. The chemical composition of amorphous components of Rocknest is 37.20 wt% SiO_2, 23.14 wt% $FeO+Fe_2O_3$, 2.09 wt% P_2O_5, and 11.01 wt% SO_3 (Blake et al. 2013). TEM-EDS results of Green Bay nodules (especially in proto-goethite rich area) also show high concentrations of these components

(~18.8 wt% SiO_2 and ~2.4 wt% P_2O_5). Thus, it is expected to have similar nanophase Fe-minerals in the two systems that the single chain structure of proto-goethite strongly able to absorb the tetrahedral anions. In addition, our Rietveld refinement result of Mars soil provides an additional cristobalite phase from the XRD pattern of Rocknest at Gale Grater (Bish et al. 2013) (Supplementary Fig. S1). The cristobalite might be resulted in by meteorite impact that locally caused by high temperature environment for shocked-melting (Chao et al. 1970).

ACKNOWLEDGMENTS

The authors would like to acknowledge the financial support from NASA Astrobiology Institute (N07-5489). Authors thank Prof. Carl Bowser for providing the samples and their locations, Dr. Hiromi Konishi for assistance in acquiring Z-contrast images. Authors also thank Professors Philip E. Brown, John W. Valley, Clark M. Johnson, Eric E. Roden, and Franklin Hobbs for their helpful suggestions.

REFERENCES CITED

Atkins, A.L., Shaw, S., and Peacock, C.L. (2014) Nucleation and growth of todorokite from birnessite: Implications for trace-metal cycling in marine sediments. Geochimica Et Cosmochimica Acta, 144, 109-125.

Barron, V., and Torrent, J. (2013) Iron, manganese and aluminium oxides and oxyhydroxides. Minerals at the Nanoscale, 14, 297-336.

Bish, D.L., Blake, D.F., Vaniman, D.T., Chipera, S.J., Morris, R.V., Ming, D.W., Treiman, A.H., Sarrazin, P., Morrison, S.M., Downs, R.T., Achilles, C.N., Yen, A.S., Bristow, T.F., Crisp, J.A., Morookian, J.M., Farmer, J.D., Rampe, E.B., Stolper, E.M., Spanovich, N., and Team, M.S. (2013) X-ray Diffraction Results from Mars Science Laboratory: Mineralogy of Rocknest at Gale Crater. Science, 341(6153).

Blake, D.F., Morris, R.V., Kocurek, G., Morrison, S.M., Downs, R.T., Bish, D., Ming, D.W., Edgett, K.S., Rubin, D., Goetz, W., Madsen, M.B., Sullivan, R., Gellert, R., Campbell, I., Treiman, A.H., McLennan, S.M., Yen, A.S., Grotzinger, J., Vaniman, D.T., Chipera, S.J., Achilles, C.N., Rampe, E.B., Sumner, D., Meslin, P.Y., Maurice, S., Forni, O., Gasnault, O., Fisk, M., Schmidt, M., Mahaffy, P., Leshin, L.A., Glavin, D., Steele, A., Freissinet, C., Navarro-Gonzalez, R., Yingst, R.A., Kah, L.C., Bridges, N., Lewis, K.W., Bristow, T.F., Farmer, J.D., Crisp, J.A., Stolper, E.M., Marais, D.J.D., Sarrazin, P., and Team, M.S. (2013) Curiosity at Gale Crater, Mars: Characterization and Analysis of the Rocknest Sand Shadow. Science, 341(6153).

Callender, E., Bowser, C.J., and Rossmann, R. (1973) Geochemistry of Ferromanganese and Manganese Carbonate Crusts from Green Bay, Lake-Michigan. Transactions-American Geophysical Union, 54(4), 340-340.

Chao, E.C.T., James, O.B., Minkin, J.A., Boreman, J.A., Jackson, E.D., and Raleigh, C.B. (1970) Petrology of Unshocked Crystalline Rocks and Shock Effects in Lunar Rocks and Minerals. Science, 167(3918), 644-647.

Chenavas, J., Joubert, J.C., Capponi, J.J., and Marezio, M. (1973) Synthesis of New Dense Phases of Oxyhydroxides M(3+)OOH of Metals of First Transition Series in High-Pressure Hydrothermal Medium. Journal of Solid State Chemistry, 6(1), 1-15.

Christensen, E.R., and Chien, N.K. (1981) Fluxes of Arsenic, Lead, Zinc, and Cadmium to Green Bay and Lake-Michigan Sediments. Environmental Science & Technology, 15(5), 553-558.

Christensen, H., and Christensen, A.N. (1978) Hydrogen-Bonds of Gamma-FeOOH. Acta Chemica Scandinavica Series a-Physical and Inorganic Chemistry, 32(1), 87-88.

Cornell, R.M., and Schwertmann, U. (2003) The iron oxides : structure, properties, reactions, occurrences, and uses. xxxix, 664 p. p. Wiley-VCH, Weinheim.

Drits, V.A., Sakharov, B.A., and Manceau, A. (1993a) Structure of Feroxyhite as Determined by Simulation of X-Ray-Diffraction Curves. Clay Minerals, 28(2), 209-222.

Drits, V.A., Sakharov, B.A., Salyn, A.L., and Manceau, A. (1993b) Structural Model for Ferrihydrite. Clay Minerals, 28(2), 185-207.

Dudarev, S.L., Botton, G.A., Savrasov, S.Y., Humphreys, C.J., and Sutton, A.P. (1998) Electron-energy-loss spectra and the structural stability of nickel oxide: An LSDA+U study. Physical Review B, 57(3), 1505-1509.

Edgingto, D., and Callender, E. (1970) Minor Element Geochemistry of Lake-Michigan Ferromanganese Nodules. Earth and Planetary Science Letters, 8(2), 97-100.

Feng, J.L., Lin, Y.C., Gao, S.P., and Zhang, J.F. (2012) Enrichment of trace elements in ferromanganese concretions from terra rossa and their potential desorption. Geochemical Journal, 46(2), 151-161.

Fontes, M.R., Weed, S.B., and Bowen, L.H. (1992) Association of Microcrystalline Goethite and Humic-Acid in Some Oxisols from Brazil. Soil Science Society of America Journal, 56(3), 982-990.

Gualtieri, A.F., and Venturelli, P. (1999) In situ study of the goethite-hematite phase transformation by real time synchrotron powder diffraction. American Mineralogist, 84(5-6), 895-904.

Handler, R.M., Beard, B.L., Johnson, C.M., and Scherer, M.M. (2009) Atom Exchange between Aqueous Fe(II) and Goethite: An Fe Isotope Tracer Study. Environmental Science & Technology, 43(4), 1102-1107.

Harrington, R., Michel, M., Parise, J., Hausner, D., and Strongin, D. (2010) Powder neutron diffraction studies of ferrihydrite, a nanocrystalline materietal. Geochimica Et Cosmochimica Acta, 74(12), A383.

Koch, C.B., Oxborrow, C.A., Morup, S., Madsen, M.B., Quinn, A.J., and Coey, J.M.D. (1995) Magnetic-Properties of Feroxyhyte (Delta-Feooh). Physics and Chemistry of Minerals, 22(5), 333-341.

Kresse, G., and Furthmuller, J. (1996) Efficient iterative schemes for ab initio total-energy calculations using a plane-wave basis set. Physical Review B, 54(16), 11169-11186.

Laberty, C., and Navrotsky, A. (1998) Energetics of stable and metastable low-temperature iron oxides and oxyhydroxides. Geochimica Et Cosmochimica Acta, 62(17), 2905-2913.

Lee, S., and Xu, H. (2016) XRD and TEM studies on Mn-oxide nano-phase minerals in freshwater ferromanganese nodules from Green Bay, Lake Michigan. American Mineralogist, (submitted).

Majzalan, J., Koch, C.B., and Navrotsky, A. (2008) Thermodynamic properties of feroxyhyte (δ'-FeOOH). Clays and Clay Minerals, 56(5), 526-530.

Manceau, A., Tamura, N., Celestre, R.S., MacDowell, A.A., Geoffroy, N., Sposito, G., and Padmore, H.A. M (2003) Molecular-Scale Speciation of Zn and Ni in Soil Ferromanganese Nodules from Loess Soils of the Mississippi Basin. Environmental Science Trachnology, 37, 75-80.

Manceau, A., Kersten, M., Marcus, M.A., Geoffroy, N., and Granina, L. (2007a) Ba and Ni speciation in a nodule of binary Mn oxide phase composition from Lake Baiketal. Geochimica Et Cosmochimica Acta, 71(8), 1967-1981.

Manceau, A., Lanson, M., and Geoffroy, N (2007b) Natural speciation of Ni, Zn, and As in ferromanganese coatings on quartz using X-ray fluorescence, absorption, and diffraction, Geochimica Et Cosmochimica Acta, 71(1), 95-128.

Manceau, A. (2009) Evaluation of the structural model for ferrihydrite derived from real-space modelling of high-energy X-ray diffraction data. Clay Minerals, 44(1), 19-34.

Manceau, A. (2011) Critical evaluation of the revised aldalatite model for ferrihydrite. American Mineralogist, 96, 521-533

Manceau, A., Lanson, M., and Takahashi, Y. (2014a) Mineralogy and crystal chemistry of Mn, Fe, Co, Ni, and Cu in a deep-sea Pacific polymetallic nodule. American Mineralogist, 99(10), 2068-2083.

Manceau, A., Skanthakumar, S., and Soderholm, L. (2014b) PDF analysis of ferrihydrite: Critical assessment of the under-constrained akdalaite model. American Mineralogist, 99(1), 102-108.

Marcus, M.A., Manceau, A., and Kersten, M. (2004) Mn, Fe, Zn and As speciation in a fast-growing ferromanganese marine nodule. Geochimica Et Cosmochimica Acta, 68(14), 3125-3136.

Michel, F.M., Ehm, L., Antao, S.M., Lee, P.L., Chupas, P.J., Liu, G., Strongin, D.R., Schoonen, M.A.A., Phillips, B.L., and Parise, J.B. (2007) The structure of ferrihydrite, a nanocrystalline materiet al. Science, 316(5832), 1726-1729.

Novikov, G.V., and Bogdanova, O.Y. (2007) Transformations of ore minerals in genetically different oceanic ferromanganese rocks. Lithology and Mineral Resources, 42(4), 303-317.

Nowlan, G.A. (1976) Concretionary Manganese-Iron Oxides in Streams and Their Usefulness as a Sample Medium for Geochemical Prospecting. Journal of Geochemical Exploration, 6(1-2), 193-210.

Palumbo, B., Bellanca, A., Neri, R., and Roe, M.J. (2001) Trace metal partitioning in Fe-Mn nodules from Sicilian soils, Italy. Chemical Geology, 173(4), 257-269.

Parise, J.B., Harrington, R., Xu, W., Michel, F.M., Hausner, D.B., Debnath, S., and Strongin, D.R. (2010) Understanding the composition and structure of ferrihydrite. Geochimica Et Cosmochimica Acta, 74(12), A793.

Pennycook, S.J., Rafferty, B., and Nellist, P.D. (2000) Z-contrast imaging in an aberration-corrected scanning transmission electron microscope. Microscopy and Microanalysis, 6(4), 343-352.

Perdew, J.P., Burke, K., and Ernzerhof, M. (1996) Generalized gradient approximation made simple. Physical Review Letters, 77(18), 3865-3868.

Pinney, N., Kubicki, J.D., Middlemiss, D.S., Grey, C.P., and Morgan, D. (2009) Density Functional Theory Study of Ferrihydrite and Related Fe-Oxyhydroxides. Chemistry of Materials, 21(24), 5727-5742.

Post, J.E., Heaney, P.J., Dreele, R.B and Hanson, J. (2003) Neutron and temperature-resolved synchroton X-ray powder diffraction study of akaganeite, 88(5), 782-788.

Robbins, J.A., and Callender, E. (1975) Diagenesis of Manganese in Lake-Michigan Sediments. American Journal of Science, 275(5), 512-533.

Rossmann, R., and Callender, E. (1968) Manganese Nodules in Lake Michigan. Science, 162(3858), 1123-1124.

Rossmann, R., and Edgington, D.N. (2000) Mercury in Green Bay, Lake Michigan surficial sediments collected between 1987 and 1990. Journal of Great Lakes Research, 26(3), 323-339.

Rosso, K.M., and Rustad, J.R. (2001) Structures and energies of AlOOH and FeOOH polymorphs from plane wave pseudopotential calculations. American Mineralogist, 86(3), 312-317.

Shen, Z.Z., Konishi, H., Szlufarska, I., Brown, P.E., and Xu, H.F. (2014) Z-contrast imaging and ab initio study on "d" superstructure in sedimentary dolomite. American Mineralogist, 99(7), 1413-1419.

Stein, L.Y., La Duc, M.T., Grundl, T.J., and Nealson, K.H. (2001) Bacterial and archaeal populations associated with freshwater ferromanganous micronodules and sediments. Environmental Microbiology, 3(1), 10-18.

Stumm, W. (1987) Aquatic surface chemistry : chemical processes at the particle-water interface. xix, 520 p. p. Wiley, New York.

Vaniman, D.T., Bish, D.L., Ming, D.W., Bristow, T.F., Morris, R.V., Blake, D.F., Chipera, S.J., Morrison, S.M., Treiman, A.H., Rampe, E.B., Rice, M., Achilles, C.N., Grotzinger, J.P., McLennan, S.M., Williams, J., Bell, J.F., Newsom, H.E., Downs, R.T., Maurice, S., Sarrazin, P., Yen, A.S., Morookian, J.M., Farmer, J.D., Stack, K., Milliken, R.E., Ehlmann, B.L., Sumner, D.Y., Berger, G., Crisp, J.A., Hurowitz, J.A., Anderson, R., Des Marais, D.J., Stolper, E.M., Edgett, K.S., Gupta, S., Spanovich, N., and Team, M.S. (2014) Mineralogy of a Mudstone at Yellowknife Bay, Gale Crater, Mars. Science, 343(6169).

Wyckoff, R.W.G (1963) Crystal structures. John Wiley Interscience Publishers, 1, 290-295.

Xu, H.F., Shen, Z.S., and Konishi, H. (2014a) Si-magnetite nano-precipitates in silician magnetite from banded iron formation: Z-contrast imaging and ab initio study. American Mineralogist, 99(11-12), 2196-2202.

Xu, H.F., Shen, Z.Z., Konishi, H., Fu, P.Q., and Szlufarska, I. (2014b) Crystal structures of laihunite and intermediate phases between laihunite-1M and fayalite: Z-contrast imaging and ab initio study. American Mineralogist, 99(5-6), 881-889.

FIGURE CAPTIONS

Figure 1. Location of Green Bay FFN samples as red dashed area on the western edge of Lake Michigan, including average Fe/Mn ratios (modified from Callender et al. 1973).

Figure 2. Optical images of hand specimens of Green Bay FFN: (A) Fe-Mn nodules and (B) Fe-rich nodules.

Figure 3. X-ray diffraction patterns of Green Bay FFN taken with 0.3 mm collimator, including natural 2-line ferrihydrite, and other reference XRD patterns. Yellow circles are the spots of XRD beam. Bus = buserite; Bir = birnessite; Fxy = feroxyhyte; Gt = goethite; Tod = todorokite; Q = quartz.

Figure 4. Bright-field TEM, SAED, HRTEM, and Z-contrast image showing nanophase Fe-oxyhydroxides: (A) the aggregates of 2-line ferrihydrite with its SAED; (B) the aggregates of 2-line ferrihydrite and goethite nanocrystals with their SAED pattern (inserted at up-right corner); (C) a HRTEM image of the Fe-oxyhydroxides showing goethite nanocrystals and feroxyhyte or proto-goethite nano-crystals; (D) a Z-contrast image of a hexagon-looking disordered Fe-oxyhydroxide (possible feroxyhyte); (E-F) X-ray EDS spectra from proto-goethite-rich and nanophase goethite-rich areas. Gt = goethite; Fxy = feroxyhyte. Weak peaks from P and As are evident in the spectrum from proto-goethite dominated area (E).

Figure 5. A [001]-zone-axis Z-contrast image showing ordered hexagonal pattern of Fe atoms: (A) Z-contrast image and its FFT pattern, and (B) a noised-filtered image of the outlined area in A. The structure model of proto-goethite is overlaid on the upper-right corner.

Figure 6. Fe, O, and H positions of goethite, proto-goethite, feroxyhyte, and hematite along [001]-zone-axis. The Fe, O, H atoms are colored in brown, red, and blue, respectively. Obviously, goethite does not match the Z-contrast image in Fig. 5.

Figure 7. (A) a [010]-zone-axis Z-contrast image showing interface between proto-

476 goethite and a stacking fault in goethite; (B) an FFT pattern from the selected area in A; (C) a
477 noise-filtered image of the outlined area in A. The unit cell models of goethite along *b*-axis
478 (left), and overlapped goethite and proto-goethite (center), and its stacking fault (right) are
479 overlaid in the image.

480 **Figure 8.** Polyhedral model of goethite (light ocher) and proto-goethite (brown) along
481 [100]-zone-axis with their atomic models along [010]-zone-axis.

482 **Figure 9.** (A) Energy differences of other FeOOH polymorphs with respect to goethite,
483 and (B) Ball-and-stick models of feroxyhyte, proto-goethite, and goethite along [100]-zone-
484 axis. The Fe, O, H atoms are colored in brown, red, and blue, respectively.

485 **Figure 10.** Polyhedral drawings of the goethite stacking fault (~1/2[**b**+**c**]) along the
486 [100]-zone-axis and ball-and-stick models along [010]-zone-axis.

487 **Figure 11.** A X-ray diffraction pattern from a Green Bay Fe-rich nodule with other
488 reference patterns: (a) a XRD pattern of Fe-rich nodule, (b) a natural nanophase goethite, (c)
489 calculated XRD pattern of feroxyhyte with particle size of 5 nm (Drits et al. 1993b), (d)
490 calculated XRD pattern of proto-goethite with particle size of 5 nm, and (e) a natural 2-line
491 ferrihydrite sample. Gt=goethite, Fxy=feroxyhyte, and Q=quartz.

492 **Figure 12.** (A) a [001]-zone-axis Z-contrast image of proto-goethite, bright spots are
493 positions of Fe atom columns. Very bright spots are As atoms on the surface right above Fe;
494 (B) the intensity profile of an outlined area from X to Y; (C) the intensity profile of simulated
495 Z-contrast image; (D) a simulated Z-contrast image; (E-F) Polyhedral models showing
496 arsenate adsorption on (001) surface of the proto-goethite.

497 **Figure 13.** Polyhedral models of (001) surface of goethite and proto-goethite with
498 tetrahedral models of arsenate (scorodite), silicate (fayalite), phosphate (apatite), and sulphate
499 (jarosite).

Table 1. Atomic coordinates and bond distance in proto-goethite based on $Pm2_1n$ setting.

Space group	$Pm2_1n$		
Atom	x	y	z
Fe	0.0000	0.9871	0.2753
H	0.0000	0.5035	0.1958
O1	0.0000	0.3246	0.4862
O2	0.0000	0.6353	0.0139
Fe-octahedra		Hydrogen bond	
Fe-O1 (2)	1.9745 Å	H-O2	1.0208 Å
Fe-O1	1.8903 Å		
Fe-O2 (2)	2.0731 Å		
Fe-O2	2.0641 Å		

Table 2. Unit-cell parameters of goethite, proto-goethite, lepidocrocite, and akaganéite.

Mineral	Space group	a/Å		diff(%)	b/Å		diff(%)	c/Å		diff(%)	β		diff(%)
		Cal.	Exp.		Cal.	Exp.		Cal.	Exp.		Cal.	Exp.	
Goethite	*Pmnb*	2.982	3.013	-1.0%	9.853	9.913	-0.6%	4.504	4.580	-1.7%			
Proto-goethite	$Pm2_1n$	2.960	2.994	-1.1%	4.898	4.937	-0.8%	4.347	4.432	-1.9%			
Lepidocrocite	*Bbmm*	3.021	3.06	-1.3%	12.132	12.40	-2.2%	3.874	3.87	0.1%			
Akaganéite	*I2/m*	10.440	10.587	-1.4%	3.011	3.031	-0.7%	10.182	10.515	-3.2%	91.054	90.020	1.1%

Notes: The experimental values for goethite, proto-goethite, lepidocrocite, and akaganéite are measured from (Gualtieri and Venturelli 1999), (Chenavas et al. 1973), (Wyckoff 1963), and (Post et al. 2003), respectively.

Table 3. The calculated energy, ZPE, and ΔG for four FeOOH polymorphs. Energies are in kJ/mol.

	E_0	ΔE	ZPE	ΔZPE	ΔG
Goethite	-2411.2010		28.6706		0
Proto-goethite	-2405.5949	5.6060	28.0239	-0.6467	4.9593
Lepidocrocite	-2397.3524	13.8486	27.8530	-0.8177	13.0309
Akaganéite	-2383.8557	27.3453	28.0181	-0.6525	26.6927

Note: E_0 is the DFT calculated energy at 0K. ΔE is the relative energy compared to the energy of goethite. ZPE is the zero point energy. ΔZPE is the relative ZPE to that of goethite. ΔG is the relative total energy (E_0 + ZPE) compared to that of goethite.

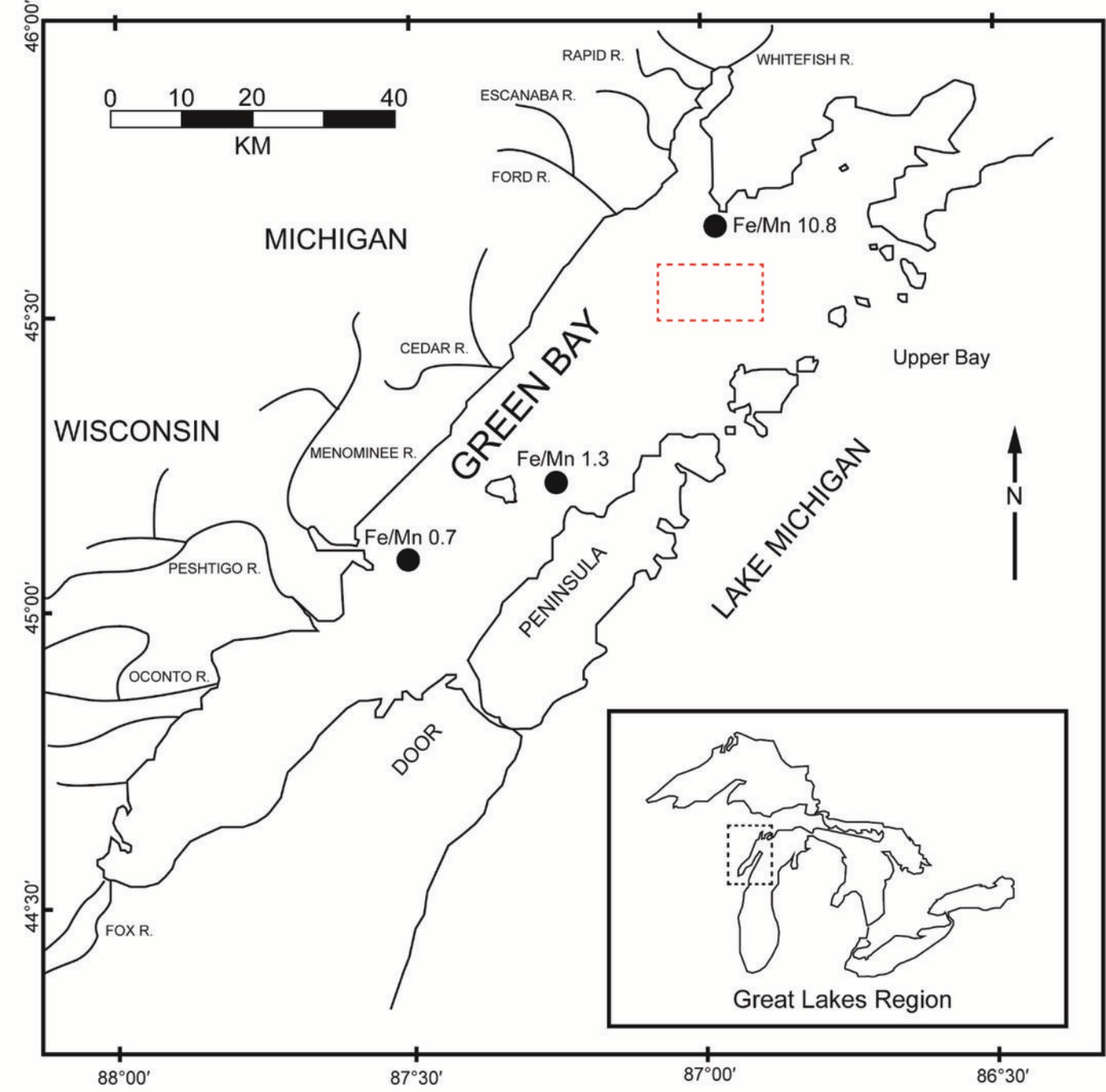
0 10 20 40
KM
RAPID R.
WHITEFISH R.
ESCANABA R.
FORD R.
MICHIGAN
Fe/Mn 10.8
CEDAR R.
GREEN BAY
Upper Bay
WISCONSIN
MENOMINEE R.
Fe/Mn 1.3
LAKE MICHIGAN
N
Fe/Mn 0.7
PESHTIGO R.
PENINSULA
OCONTO R.
DOOR
FOX R.
Great Lakes Region
46°00′
45°30′
45°00′
44°30′
88°00′
87°30′
87°00′
86°30′

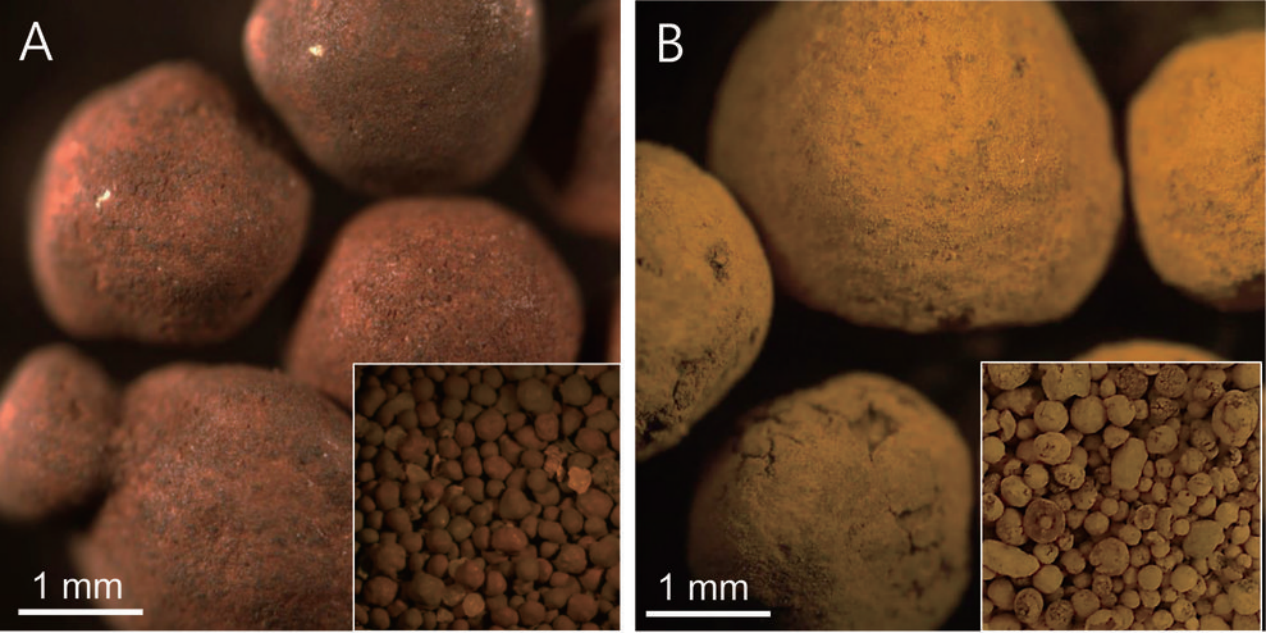
A
1 mm
B
1 mm

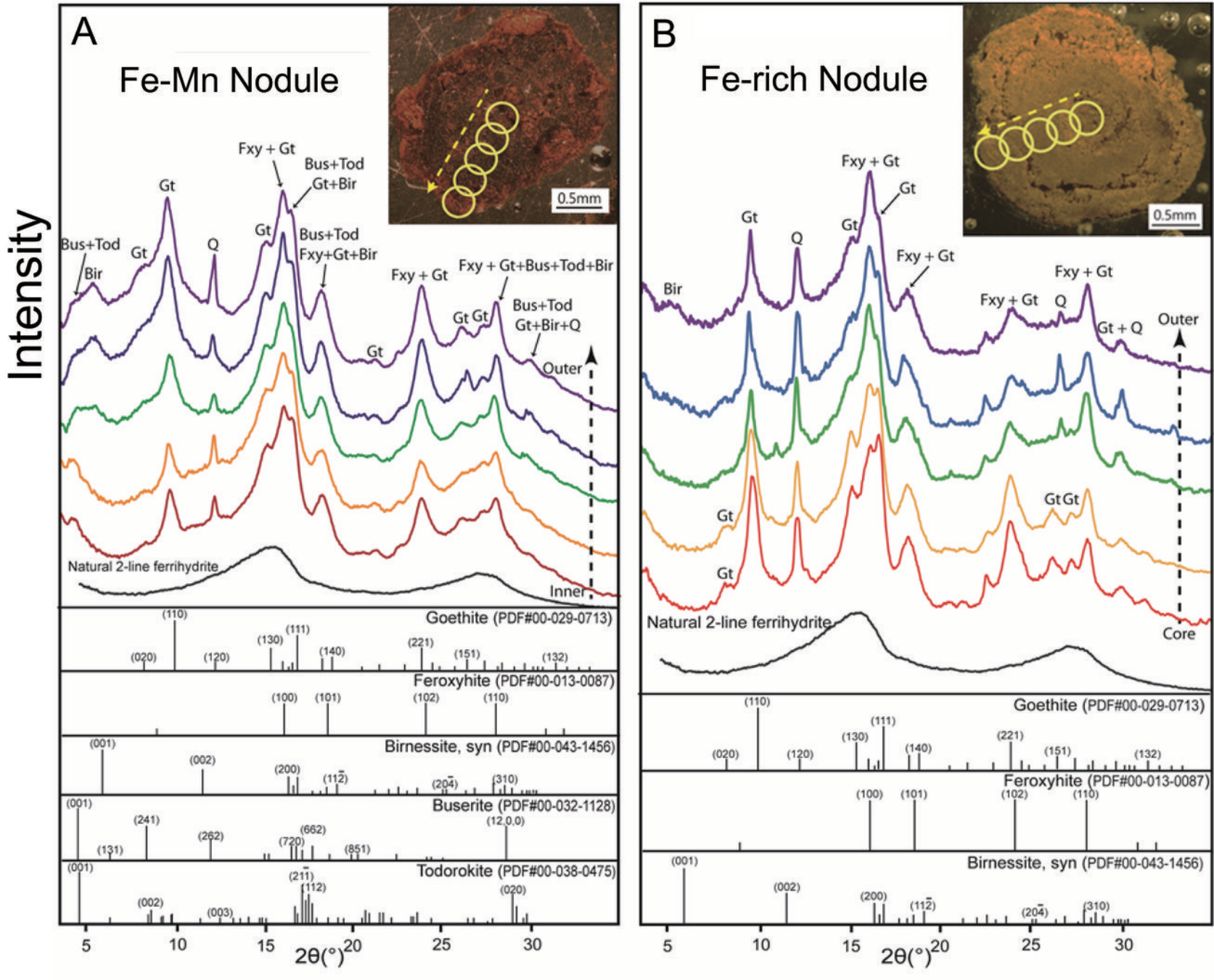
A
Fe-Mn Nodule
0.5mm
Intensity
Fxy + Gt
Bus+Tod
Gt+Bir
Gt
Bus+Tod
Gt
Q
Gt
Bus+Tod
Fxy+Gt+Bir
Bir
Fxy + Gt
Fxy + Gt+Bus+Tod+Bir
Gt Gt
Bus+Tod
Gt+Bir+Q
Gt
Outer
Natural 2-line ferrihydrite
Inner
Goethite (PDF#00-029-0713)
(110)
(020)
(120)
(130)
(111)
(140)
(221)
(151)
(132)
Feroxyhite (PDF#00-013-0087)
(100)
(101)
(102)
(110)
Birnessite, syn (PDF#00-043-1456)
(001)
(002)
(200)
(11$\bar{2}$)
(20$\bar{4}$)
(310)
Buserite (PDF#00-032-1128)
(001)
(241)
(131)
(262)
(662)
(720)
(851)
(12,0,0)
Todorokite (PDF#00-038-0475)
(001)
(002)
(003)
(21$\bar{1}$)
(112)
(020)
5
10
15
2θ(°)
20
25
30
B
Fe-rich Nodule
0.5mm
Fxy + Gt
Gt
Gt
Q
Gt
Fxy + Gt
Bir
Fxy + Gt
Fxy + Gt
Q
Gt + Q
Outer
Gt Gt
Gt
Gt
Natural 2-line ferrihydrite
Core
Goethite (PDF#00-029-0713)
(110)
(020)
(120)
(130)
(111)
(140)
(221)
(151)
(132)
Feroxyhite (PDF#00-013-0087)
(100)
(101)
(102)
(110)
Birnessite, syn (PDF#00-043-1456)
(001)
(002)
(200)
(11$\bar{2}$)
(20$\bar{4}$)
(310)
5
10
15
2θ(°)
20
25
30

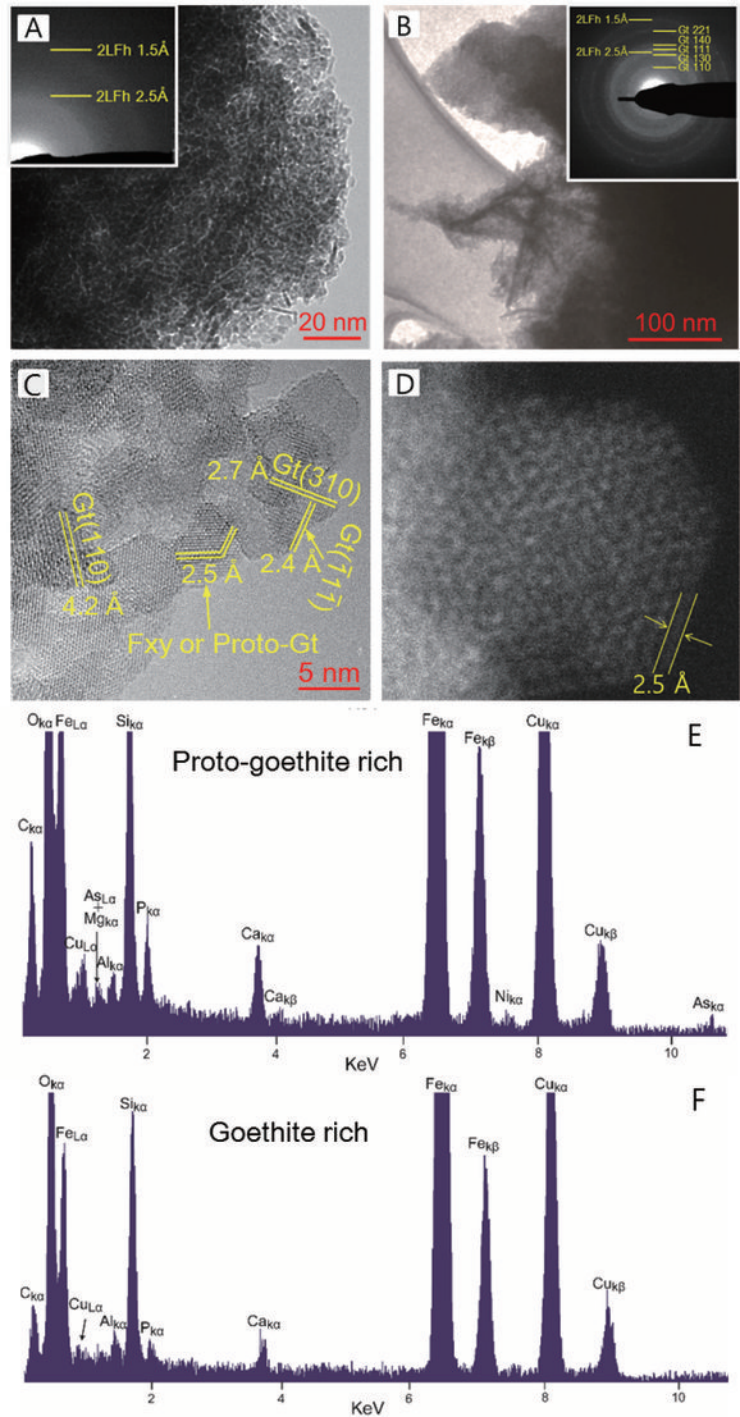
A
2LFh 1.5Å
2LFh 2.5Å
20 nm
B
2LFh 1.5Å
2LFh 2.5Å
Gt 221
Gt 140
Gt 111
Gt 130
Gt 110
100 nm
C
2.7 Å
Gt(310)
Gt(111)
2.4 Å
Gt(110)
4.2 Å
2.5 Å
Fxy or Proto-Gt
5 nm
D
2.5 Å
E
Proto-goethite rich
Oκα
FeLα
Siκα
Feκα
Feκβ
Cuκα
Cκα
AsLα + MgKα
Pκα
CuLα
AlKα
Caκα
Caκβ
Cuκβ
Niκα
Asκα
KeV
F
Goethite rich
Oκα
Siκα
FeLα
Feκα
Feκβ
Cuκα
Cκα
CuLα
AlKα
Pκα
Caκα
Cuκβ
KeV

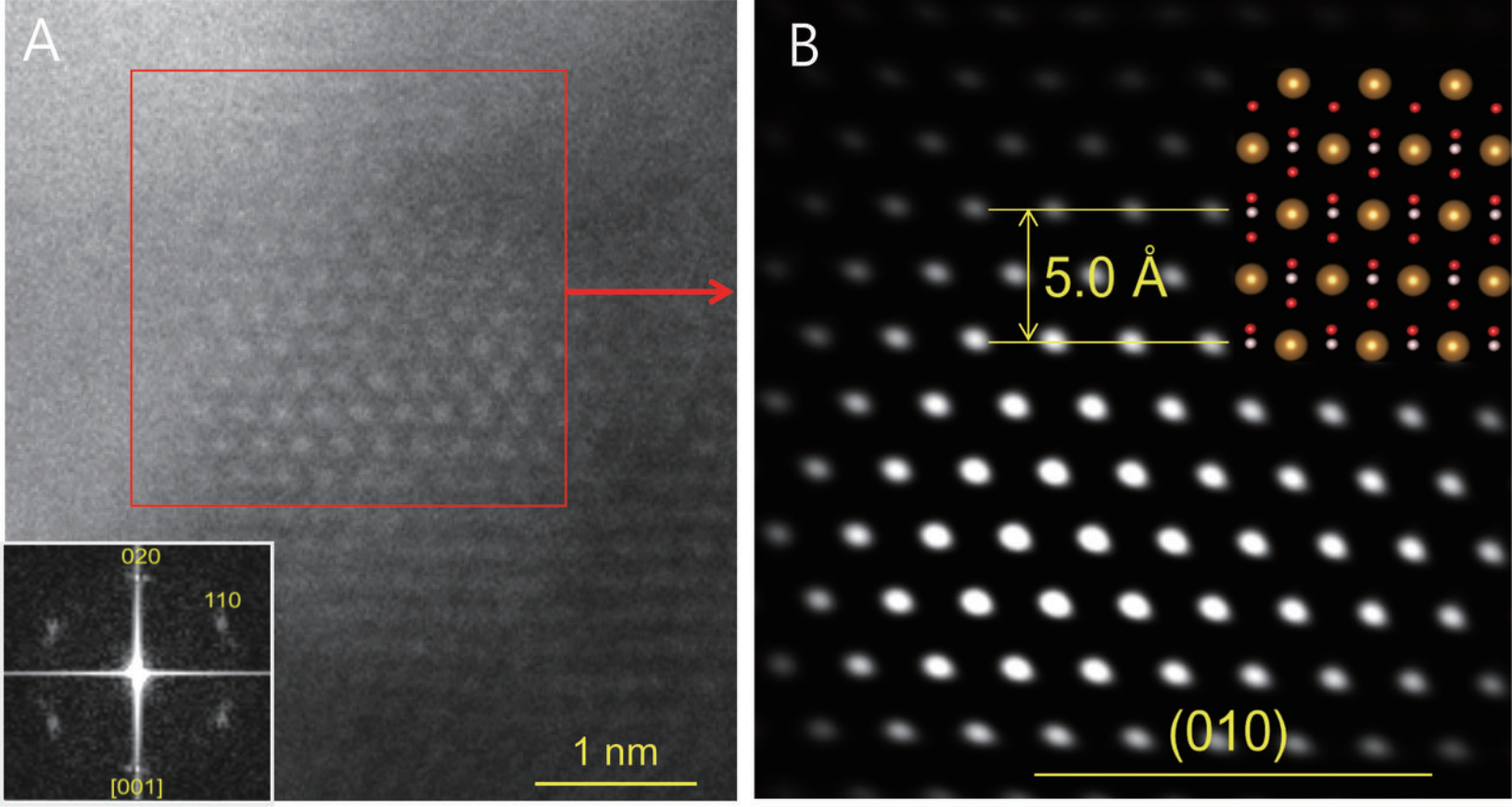
A
020
110
[001]
1 nm
B
5.0 Å
(010)

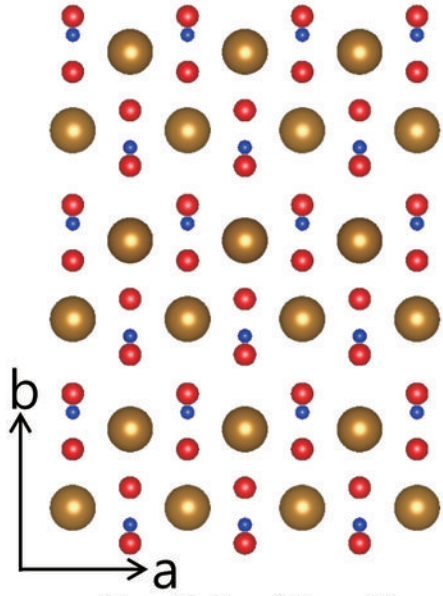

Goethite (*Pmnb*)

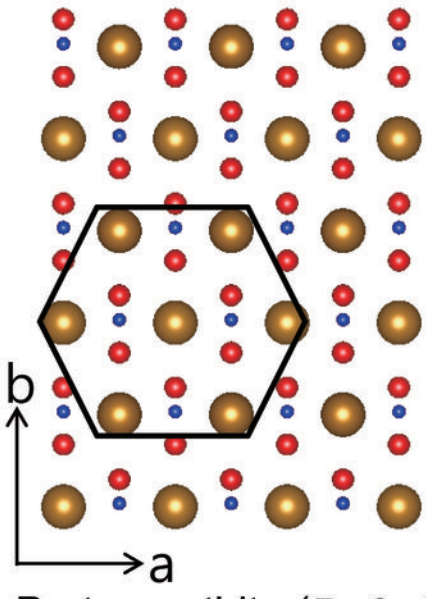

Proto-goethite ($Pm2_1n$)

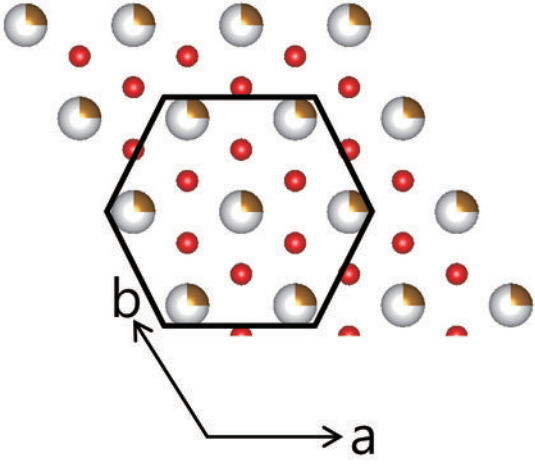

Feroxyhyte ($P\bar{3}m1$)

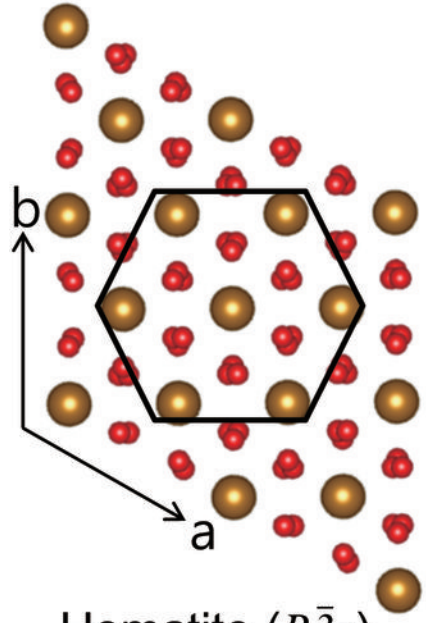

Hematite ($R\bar{3}c$)

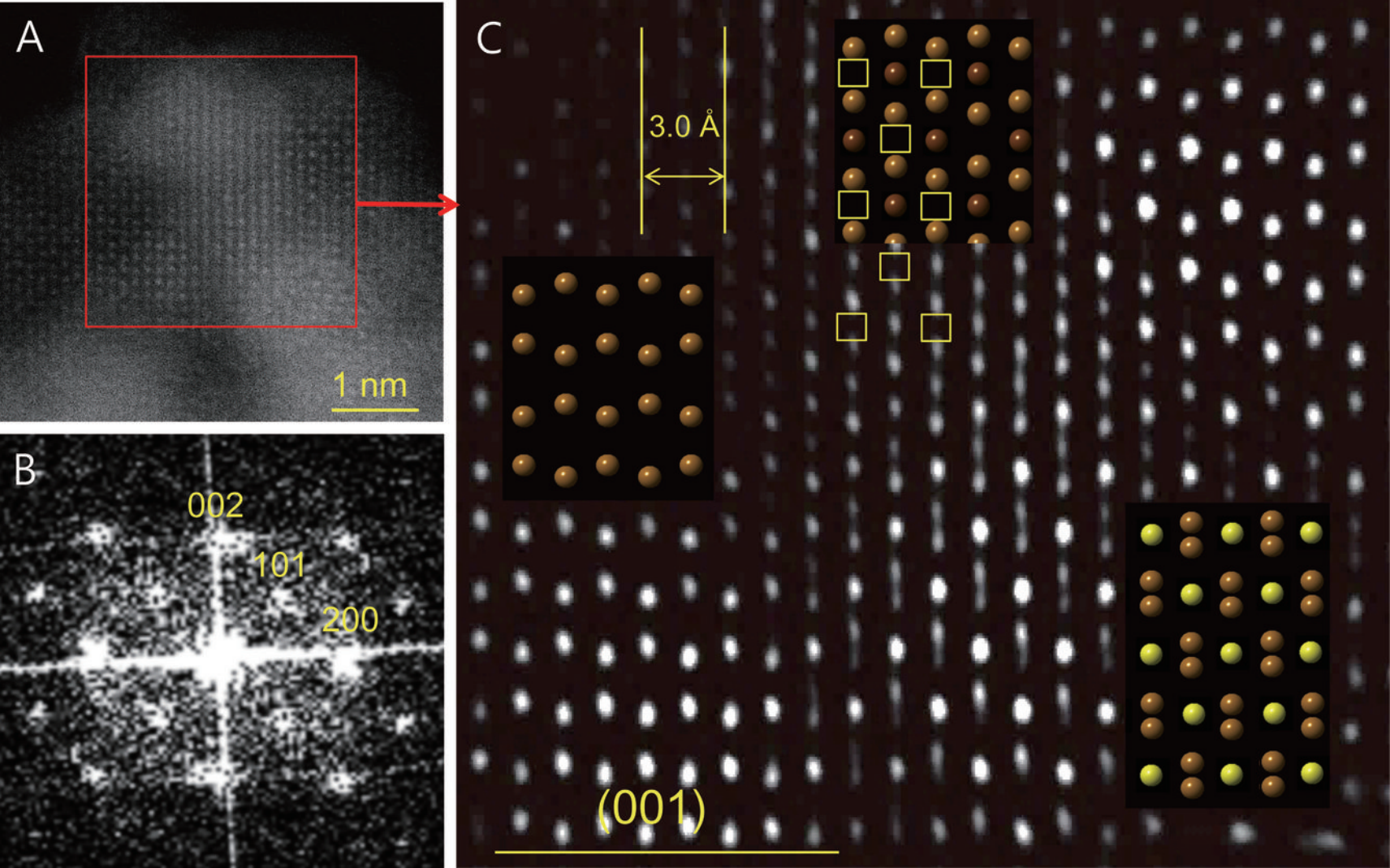
A
1 nm
B
002
101
200
C
3.0 Å
(001)

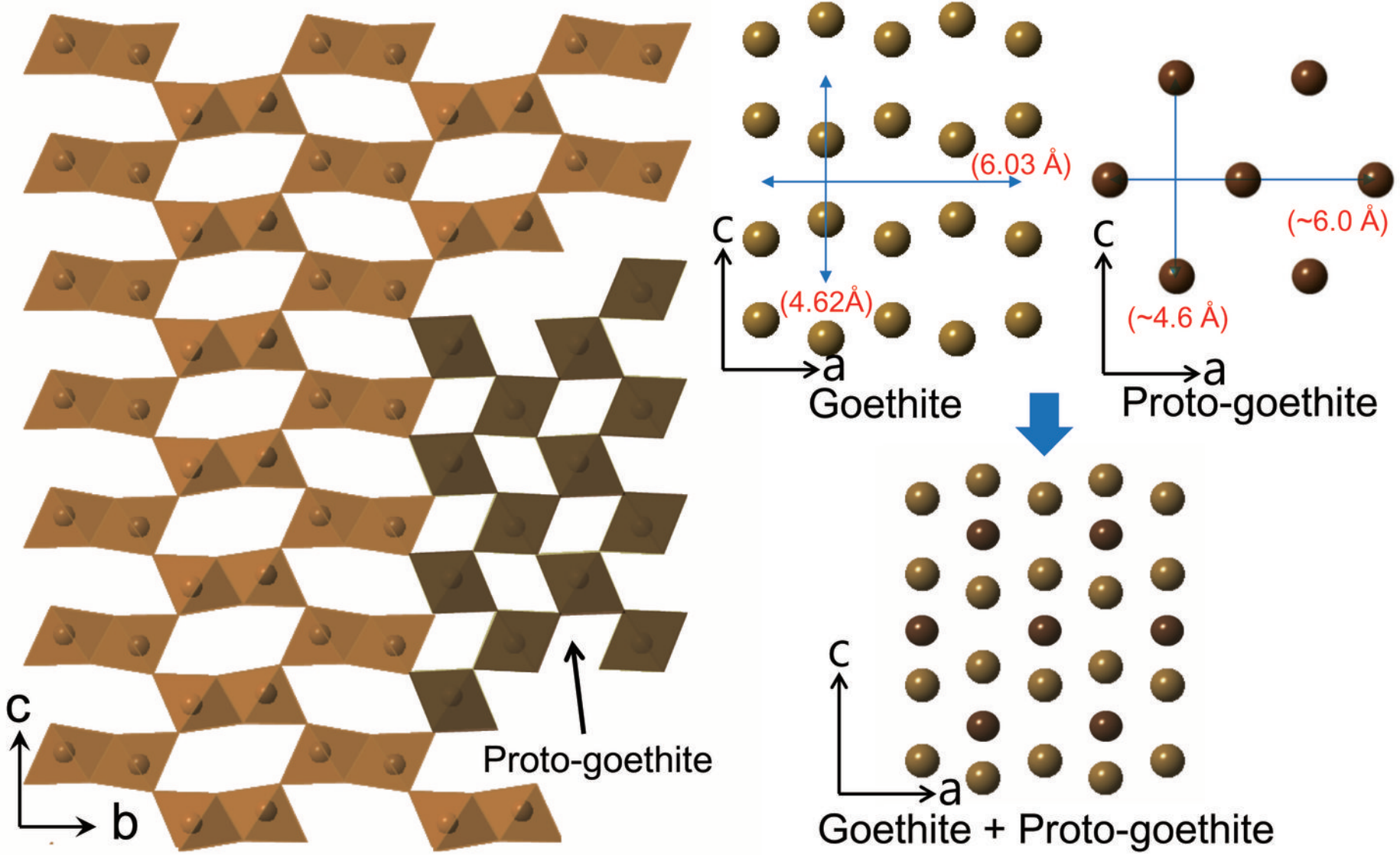
c
b
Proto-goethite
(6.03 Å)
(4.62Å)
c
a
Goethite
(~6.0 Å)
(~4.6 Å)
c
a
Proto-goethite
c
a
Goethite + Proto-goethite

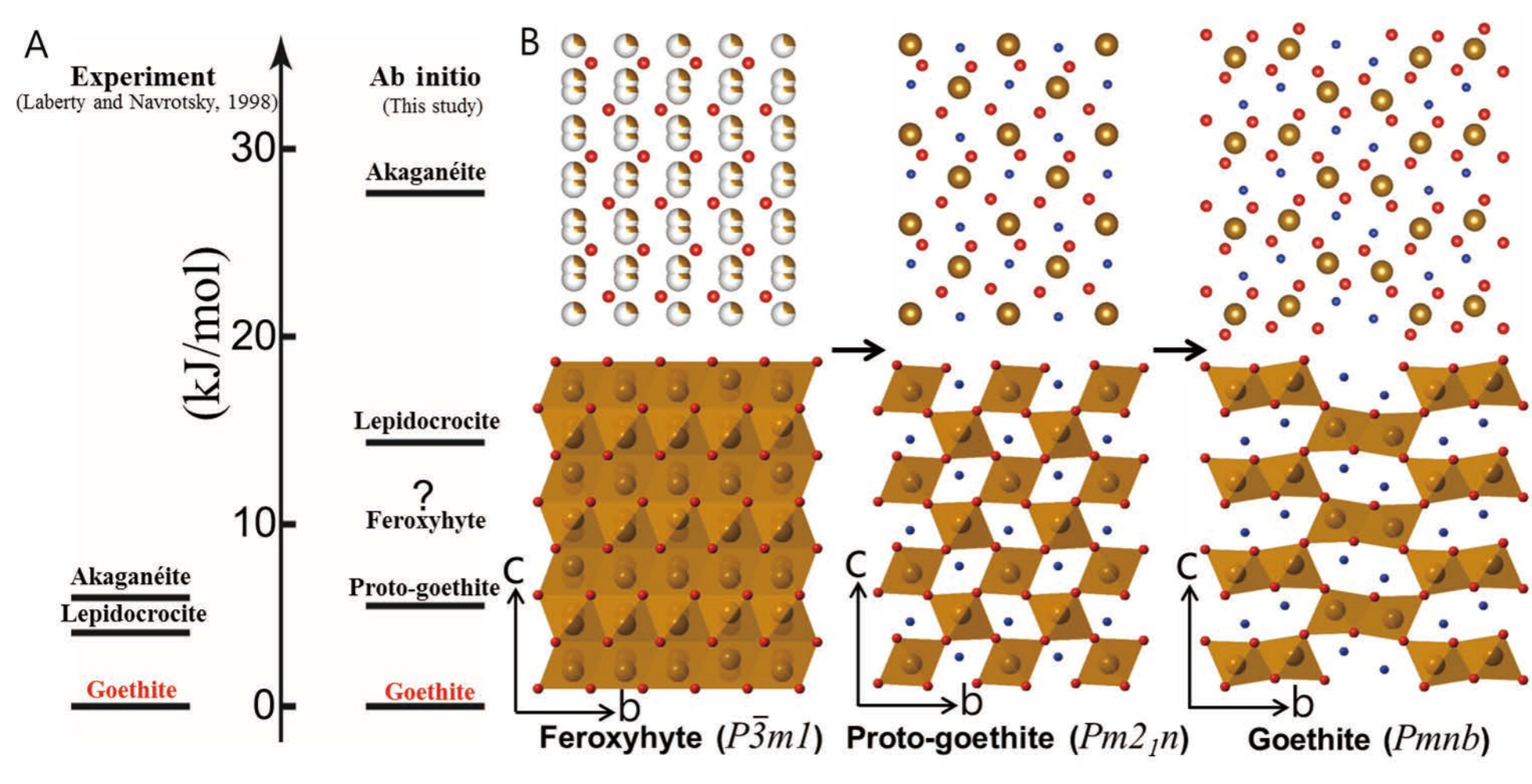
A
Experiment
(Laberty and Navrotsky, 1998)
(kJ/mol)
30
20
10
0
Akaganéite
Lepidocrocite
Goethite
Ab initio
(This study)
Akaganéite
Lepidocrocite
?
Feroxyhyte
Proto-goethite
Goethite
B
c
b
Feroxyhyte ($P\bar{3}m1$)
Proto-goethite ($Pm2_1n$)
Goethite ($Pmnb$)

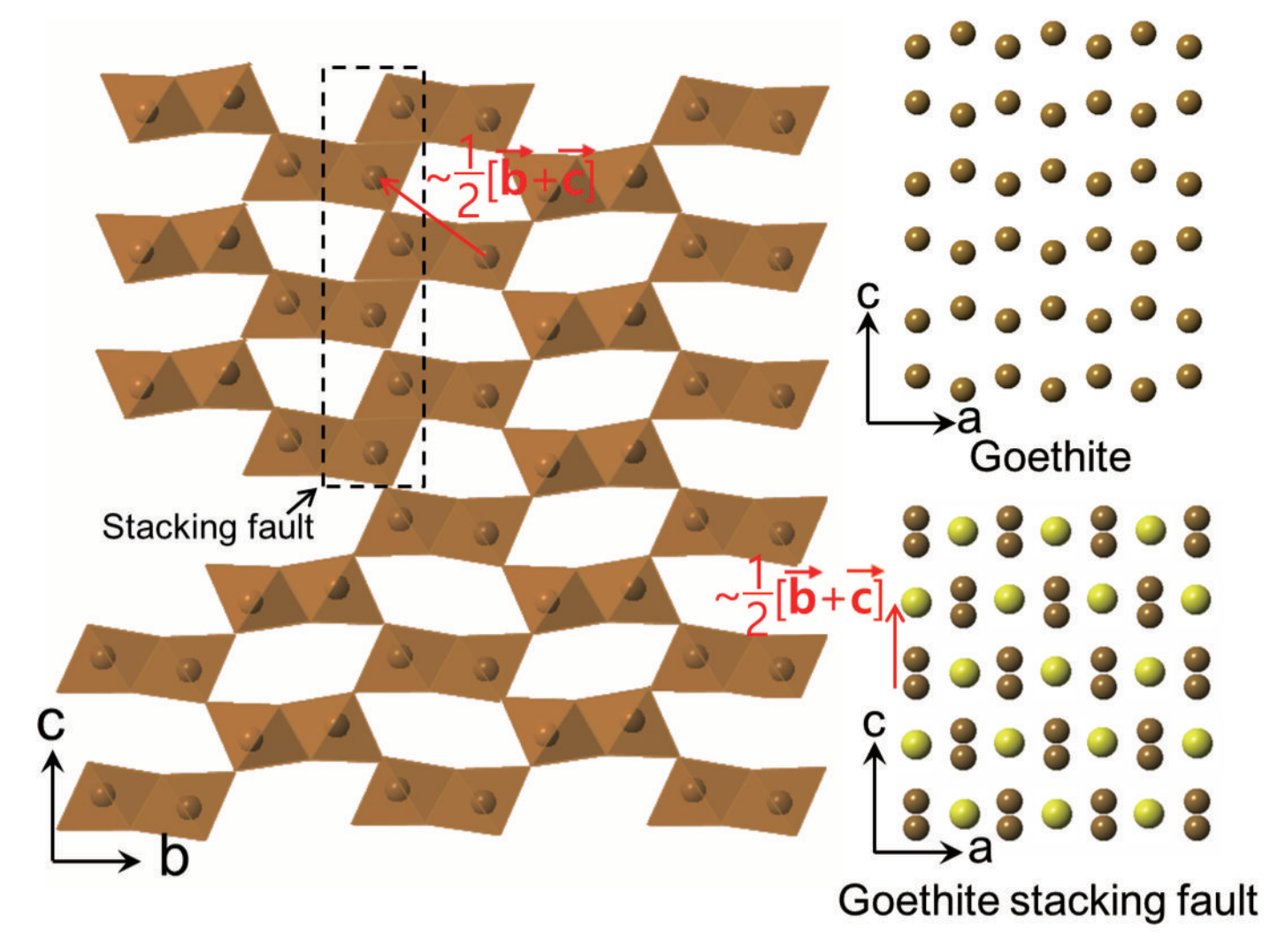
~1/2[b+c]
Stacking fault
c
b
c
a
Goethite
~1/2[b+c]
c
a
Goethite stacking fault

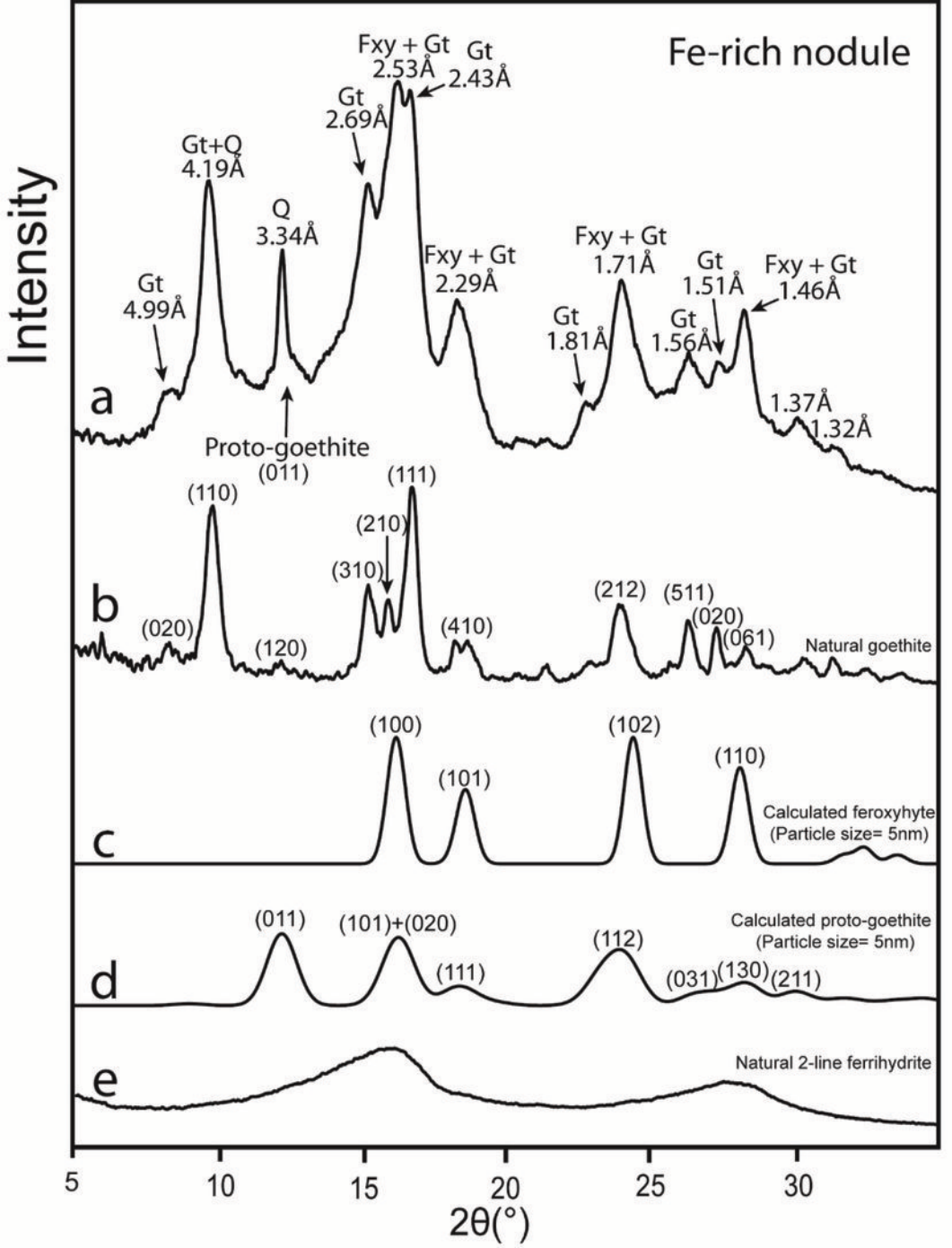
Fe-rich nodule
Intensity
a
Gt
4.99Å
Gt+Q
4.19Å
Q
3.34Å
Gt
2.69Å
Fxy + Gt
2.53Å
Gt
2.43Å
Fxy + Gt
2.29Å
Gt
1.81Å
Fxy + Gt
1.71Å
Gt
1.56Å
Gt
1.51Å
Fxy + Gt
1.46Å
1.37Å
1.32Å
Proto-goethite
(011)
b
(110)
(020)
(120)
(210)
(310)
(111)
(410)
(212)
(511)
(020)
(061)
Natural goethite
c
(100)
(101)
(102)
(110)
Calculated feroxyhyte
(Particle size= 5nm)
d
(011)
(101)+(020)
(111)
(112)
(031)
(130)
(211)
Calculated proto-goethite
(Particle size= 5nm)
e
Natural 2-line ferrihydrite
5
10
15
20
25
30
2θ(°)

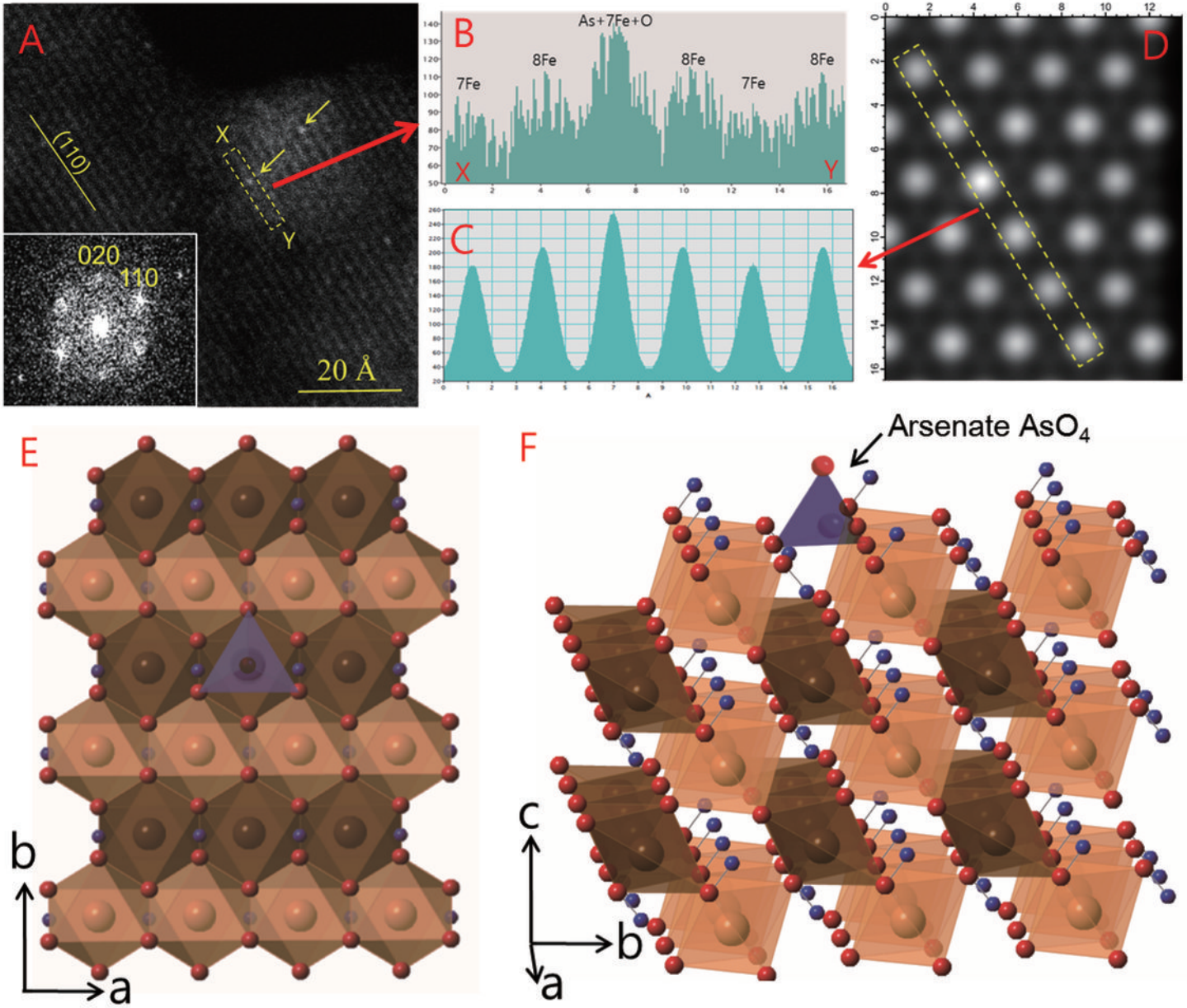
A
(110)
X
Y
020
110
20 Å
B
As+7Fe+O
8Fe
8Fe
8Fe
7Fe
7Fe
X
Y
C
D
E
b
a
F
Arsenate AsO4
c
b
a

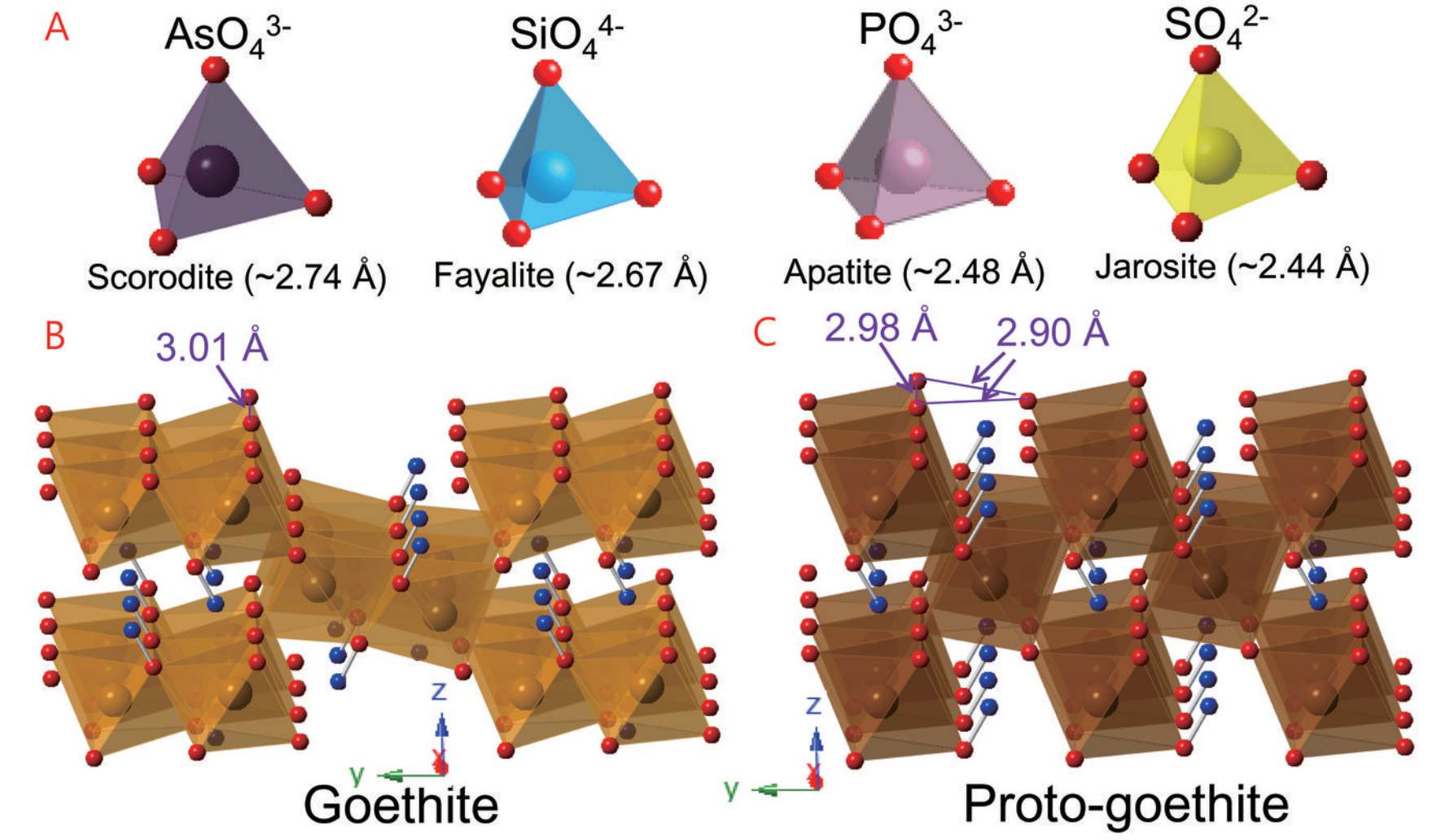
A
AsO_4^{3-}
SiO_4^{4-}
PO_4^{3-}
SO_4^{2-}
Scorodite (~2.74 Å)
Fayalite (~2.67 Å)
Apatite (~2.48 Å)
Jarosite (~2.44 Å)
B
3.01 Å
z
y
Goethite
C
2.98 Å
2.90 Å
z
y
Proto-goethite